

Collapse of magnetized hypermassive neutron stars in general relativity: Disk evolution and outflows

Branson C. Stephens,* Stuart L. Shapiro,† and Yuk Tung Liu

Department of Physics, University of Illinois at Urbana-Champaign, Urbana, IL 61801, USA

We study the evolution in axisymmetry of accretion disks formed self-consistently through collapse of magnetized hypermassive neutron stars to black holes. Such stars can arise following the merger of binary neutron stars. They are differentially rotating, dynamically stable, and have rest masses exceeding the mass limit for uniform rotation. However, hypermassive neutron stars are secularly unstable to collapse due to MHD-driven angular momentum transport. The rotating black hole which forms in this process is surrounded by a hot, massive, magnetized torus and a magnetic field collimated along the spin axis. This system is a candidate for the central engine of a short-hard gamma-ray burst (GRB). Our code integrates the coupled Einstein-Maxwell-MHD equations and is used to follow the collapse of magnetized hypermassive neutron star models in full general relativity until the spacetime settles down to a quasi-stationary state. We then employ the Cowling approximation, in which the spacetime is frozen, to track the subsequent evolution of the disk. This approximation allows us to greatly extend the disk evolutions and study the resulting outflows, which may be relevant to the generation of a GRB. We find that outflows are suppressed when a stiff equation of state is assumed for low density disk material and are sensitive to the initial magnetic field configuration.

PACS numbers: 04.25.Dm, 04.30.-w, 04.40.Dg

I. INTRODUCTION

Binary neutron star coalescence has been proposed for many years as an explanation of short-hard GRBs [1, 2]. Possible associations between short GRBs and elliptical galaxies reported recently [3] make it unlikely that short GRBs are related to collapse of massive stars and supernovae. The merger of compact-object binaries (neutron star-neutron star or black hole-neutron star) is now the favored hypothesis for explaining short GRBs. According to this scenario, the merger results in the formation of a stellar-mass black hole surrounded by a hot accretion torus which contains ~ 1 –10% of the total mass of the system. Energy extracted from this system, either by MHD processes or neutrino-radiation, powers the GRB fireball. The viability of this model depends in part on the presence of a sufficiently massive accretion disk following collapse and on whether the accretion flow produces sufficiently energetic outflows.

Instead of directly collapsing to a black hole, some binary neutron star (NS) mergers could form hypermassive neutron stars (HMNSs) as an intermediate state. Such stars are supported against collapse by strong differential rotation [4, 5, 6], which naturally arises from the merger [7, 8, 9]. The latest binary NS merger simulations in full general relativity [10, 11, 12] have confirmed that HMNS formation is indeed a possible outcome. We note, however, that HMNSs could also result from core

collapse of massive stars, since collapse generates strong differential rotation [13, 14] (see also [15]).

Differentially rotating stars tend to approach rigid rotation when acted upon by processes which transport angular momentum. HMNSs, however, cannot settle down to rigidly rotating NSs since their masses exceed the maximum allowed by rigid rotation. These objects thus undergo ‘delayed’ collapse to a black hole (BH). Several processes can act to transport angular momentum and drive the HMNS to collapse. For example, previous calculations in full general relativity have modeled HMNS evolution driven by viscous angular momentum transport [16] and by angular momentum loss due to gravitational radiation [11].

HMNS collapse due to magnetic field effects has recently been studied numerically in [17, 18, 19] using codes for evolving magnetized fluids in full general relativity [20, 21] (see also [22, 23, 24]). The secular angular momentum transport in this case is provided by two primary MHD effects. The magnetic winding effect [25] refers to the twisting of “frozen-in” magnetic field lines by a shear flow. The resulting magnetic stresses transport angular momentum so as to drive the fluid toward uniform rotation. This magnetic braking occurs on the Alfvén timescale [26], which is typically much longer than the dynamical time. In contrast to this smooth winding process, the magnetorotational instability (MRI) [27, 28] leads to exponential growth of field line distortions on a timescale comparable to the rotation period. The nonlinear outcome of this instability is MHD turbulence, which enhances angular momentum transport. Thus, magnetic braking and the MRI ultimately lead to collapse of the HMNS and the formation of a hot, magnetized accretion disk surrounding the central BH. This hot disk produces copious $\nu\bar{\nu}$ pairs, and the resulting annihilation energy

*Present address: Princeton Center for Theoretical Physics, Princeton, NJ 08544

†Also at the Department of Astronomy and NCSA, University of Illinois at Urbana-Champaign, Urbana, IL 61801

is roughly commensurate with the requirements for a short-hard GRB (as long as the emission is somewhat beamed) [18].

In addition to $\nu\bar{\nu}$ pairs, MHD processes have also been suggested as mechanisms of powering GRBs. In this paper, we explore the possibility of MHD-induced jet formation by simulating the self-consistent formation of disks through HMNS collapse in full general relativity, continuing the disk evolution for up to $\sim 2000M$ after the collapse, and examining the physical processes at work. The long duration of these simulations is achieved by using the Cowling approximation (in which the spacetime metric is fixed) following the phase of black hole excision and live evolution of the spacetime metric. (We note that by imposing the Cowling approximation, we cannot take into account changes in the metric due to the rearrangement of mass in the disk and/or accretion. However, we find that the change in disk mass during the Cowling phase is $\lesssim 3\%$ of the total mass in all of the cases we study. Hence, the Cowling approximation is expected to be fairly accurate.) We also demonstrate our code's ability to handle magnetized accretion flows in stationary spacetimes by reproducing the results of [29] for accretion of a magnetized Fishbone-Moncrief torus [30] onto a fixed Kerr BH. The good agreement of our results with the published results provides confidence in our code's ability to handle complex MHD accretion scenarios.

While the HMNS calculations presented here employ the Cowling approximation for the late phases of the evolution, we emphasize that these runs are performed using a code capable of handling *dynamical* spacetimes. Using the Cowling approximation allows us to probe the quasi-stationary behavior at much later times than presented in our earlier study [19]. We also note that the final spacetime is more general than the Kerr spacetime (our code allows for the presence of a massive accretion disk). Accretion disk dynamics in such a spacetime have not been explored by previous fixed-background *stationary* spacetime GRMHD simulations.

The evolution of accretion flows around BHs in stationary spacetimes and the consequent jet formation has been studied numerically by several groups [29, 31, 32, 33, 34, 35, 36]. The initial data for the studies of McKinney and Gammie [29] and of De Villiers *et al.* [31] consist of thick tori with weak poloidal field loops surrounding Kerr BHs of varying spins. The magnetic field is subject to the MRI, and the resulting MHD turbulence drives accretion onto the central BH. Magnetic field lines carried into the BH open outward and take on a stationary, split-monopole like structure. A relativistic, Poynting dominated outflow develops in this funnel region, while a mildly relativistic, matter dominated outflow moves along the outer edge of the funnel. McKinney [34] considered the evolution of these outflows as they propagate to large radius and found that the terminal Lorentz factors for the inner, fast jet range up to $\sim 10^3$, easily accommodating observational constraints on GRB jets. McKinney also showed that the opening angle of the outflow is con-

trolled at small radii by the corona pressure, at intermediate radii by the funnel wall outflow, and at large distances by internal magnetic stresses. In contrast, Mizuno *et al.* [35] consider a thin, Keplerian disk threaded by a uniform, vertical magnetic field. Accretion onto the BH again leads to a faster inner jet and a slower outer jet, though both are mildly relativistic.

In this paper, we find that HMNS collapse leads to a magnetically dominated funnel region surrounded (in some cases) by a mildly relativistic, unbound outflow. This flow has a similar morphology to those of the magnetized accretion disk simulations in stationary spacetimes described above [29, 31]. Though we do not find a Poynting-dominated jet in the funnel, the evolution in this region is sensitive to the numerical handling of matter in highly magnetically dominated regimes. As discussed in [20], accurate evolution in such regions is a significant challenge.

Below, we first give a brief description of our formulation and numerical methods. In Section III, we present results for the evolution of a magnetized torus surrounding a Kerr BH, following [29]. We describe our results for disk evolution following HMNS collapse in Section IV and summarize in Section V.

II. FORMULATION

A. Basic equations and numerical methods

The formulation and numerical scheme for our general relativistic, magnetohydrodynamic (GRMHD) simulations are the same as those reported in [20], to which the reader may refer for details. Here we briefly summarize the method and introduce our notation. We assume geometrized units ($G = c = 1$) except where stated explicitly.

We adopt the Baumgarte-Shapiro-Shibata-Nakamura (BSSN) formalism [37] to evolve the spacetime metric. In this formalism, the evolution variables are the conformal exponent $\phi \equiv \ln \gamma/12$, the conformal 3-metric $\tilde{\gamma}_{ij} = e^{-4\phi}\gamma_{ij}$, three auxiliary functions $\tilde{\Gamma}^i \equiv -\tilde{\gamma}^{ij}{}_{,j}$, the trace of the extrinsic curvature K , and the tracefree part of the conformal extrinsic curvature $\tilde{A}_{ij} \equiv e^{-4\phi}(K_{ij} - \gamma_{ij}K/3)$. Here, $\gamma = \det(\gamma_{ij})$, and γ_{ij} is the spatial 3-metric. The full spacetime metric $g_{\mu\nu}$ is related to the three-metric $\gamma_{\mu\nu}$ by $\gamma_{\mu\nu} = g_{\mu\nu} + n_\mu n_\nu$, where the future-directed, time-like unit vector n^μ normal to the time slice can be written in terms of the lapse α and shift β^i as $n^\mu = \alpha^{-1}(1, -\beta^i)$.

In this paper, we assume both equatorial and axisymmetry, and so we only evolve the region with $x > 0$ (where x represents the cylindrical radius ϖ) and $z > 0$. We adopt the Cartoon method [38] to impose axisymmetry in the metric evolution, and use a cylindrical grid to evolve the MHD and Maxwell equations. For the gauge conditions, we adopt hyperbolic driver conditions as in [39] to evolve the lapse α and shift β^i .

The fundamental variables in ideal MHD are the rest-mass density ρ , specific internal energy ε , pressure P , four-velocity u^μ , and magnetic field B^μ measured by a normal observer moving with a 4-velocity n^μ (note that $B^\mu n_\mu = 0$). During the evolution, we also need the three-velocity $v^i = u^i/u^t$. The ideal MHD condition is written as $u_\mu F^{\mu\nu} = 0$, where $F^{\mu\nu}$ is the electromagnetic tensor. The tensor $F^{\mu\nu}$ and its dual in the ideal MHD approximation are given by

$$F^{\mu\nu} = \epsilon^{\mu\nu\alpha\beta} u_\alpha b_\beta, \quad (1)$$

$$F_{\mu\nu}^* \equiv \frac{1}{2} \epsilon_{\mu\nu\alpha\beta} F^{\alpha\beta} = b_\mu u_\nu - b_\nu u_\mu, \quad (2)$$

where $\epsilon_{\mu\nu\alpha\beta}$ is the Levi-Civita tensor. Here we have introduced an auxiliary magnetic 4-vector $b^\mu = B_{(u)}^\mu/\sqrt{4\pi}$, where $B_{(u)}^\mu$ is the magnetic field measured by an observer comoving with the fluid and is related to B^μ by

$$B_{(u)}^\mu = -\frac{(\delta^\mu_\nu + u^\mu u_\nu) B^\nu}{n_\lambda u^\lambda}. \quad (3)$$

The energy-momentum tensor is written as

$$T_{\mu\nu} = T_{\mu\nu}^{\text{Fluid}} + T_{\mu\nu}^{\text{EM}}, \quad (4)$$

where $T_{\mu\nu}^{\text{Fluid}}$ and $T_{\mu\nu}^{\text{EM}}$ denote the fluid and electromagnetic pieces of the stress-energy tensor. They are given by

$$T_{\mu\nu}^{\text{Fluid}} = \rho h u_\mu u_\nu + P g_{\mu\nu}, \quad (5)$$

$$\begin{aligned} T_{\mu\nu}^{\text{EM}} &= \frac{1}{4\pi} \left(F_{\mu\sigma} F_\nu^\sigma - \frac{1}{4} g_{\mu\nu} F_{\alpha\beta} F^{\alpha\beta} \right) \\ &= \left(\frac{1}{2} g_{\mu\nu} + u_\mu u_\nu \right) b^2 - b_\mu b_\nu, \end{aligned} \quad (6)$$

where $h \equiv 1 + \varepsilon + P/\rho$ is the specific enthalpy, and $b^2 \equiv b^\mu b_\mu$. Hence, the total stress-energy tensor becomes

$$T_{\mu\nu} = (\rho h + b^2) u_\mu u_\nu + \left(P + \frac{b^2}{2} \right) g_{\mu\nu} - b_\mu b_\nu. \quad (7)$$

The magnetic pressure is defined as suggested by the second term in the above equation: $P_{\text{mag}} \equiv b^2/2$.

In our numerical implementation of the GRMHD and magnetic induction equations, we evolve the following conserved variables:

$$\rho_* \equiv -\sqrt{\gamma} \rho n_\mu u^\mu, \quad (8)$$

$$\tilde{S}_i \equiv -\sqrt{\gamma} T_{\mu\nu} n^\mu \gamma^\nu_i, \quad (9)$$

$$\tilde{\tau} \equiv \sqrt{\gamma} T_{\mu\nu} n^\mu n^\nu - \rho_*, \quad (10)$$

$$\mathcal{B}^i \equiv \sqrt{\gamma} B^i. \quad (11)$$

The evolution equations are integrated in conservative form using a high-resolution shock-capturing (HRSC) scheme. Specifically, we use the monotized central (MC) scheme [40] for data reconstruction and the HLL (Harten, Lax and van-Leer) scheme [41] to compute the

flux. The magnetic field \mathcal{B}^i must satisfy the no-monopole constraint $\partial_i \mathcal{B}^i = 0$. Thus, we adopt the flux-constrained transport (flux-CT) scheme [42]. In this scheme, the induction equation is differenced in such a way that a second-order, corner-centered representation of the divergence is preserved as a numerical identity. As in [19], we apply outer boundary conditions on the primitive variables ρ, P, v^i , and B^i . Outflow boundary conditions are imposed on the hydrodynamic variables (i.e., the variables are copied along the grid directions with the condition that the velocities be positive or zero in the outer grid zones). The magnetic field is linearly interpolated onto the boundaries. Finally, the conserved variables are recomputed on the boundary.

At each timestep, the primitive variables (ρ, P, v^i) must be computed from the evolution variables $(\rho_*, \tilde{\tau}, \tilde{S}_i)$. This is done by numerically solving the algebraic equations (8)–(10) together with an equation of state (EOS), $P = P(\rho, \varepsilon)$. We perform evolutions with two types of EOS. For the Fishbone-Moncrief disk [30] in Section III as well as one of the HMNS models (star A, see Section IV A), we use the Γ -law EOS:

$$P = (\Gamma - 1)\rho\varepsilon. \quad (12)$$

The corresponding cold EOS is a simple polytrope, $P_{\text{cold}} = K\rho^\Gamma$, where K is a constant. For the second HMNS model (star C in Section IV A), we assume a more realistic hybrid EOS [13, 21], in which the total pressure is written as a sum of cold and thermal parts

$$P = P_{\text{cold}} + P_{\text{th}} \quad (13)$$

The cold contribution to the pressure depends only on the density, and is defined as follows:

$$P_{\text{cold}} = \begin{cases} K_1 \rho^{\Gamma_1} & \text{for } \rho \leq \rho_{\text{nuc}} \\ K_2 \rho^{\Gamma_2} & \text{for } \rho \geq \rho_{\text{nuc}} \end{cases}. \quad (14)$$

We set $\Gamma_1 = 1.3$, $\Gamma_2 = 2.75$, $K_1 = 5.16 \times 10^{14}$ cgs, $K_2 = K_1 \rho_{\text{nuc}}^{\Gamma_1 - \Gamma_2}$, and $\rho_{\text{nuc}} = 1.8 \times 10^{14}$ g/cm³. This EOS has the desirable property that the dependence of pressure on density stiffens above nuclear density and the resulting maximum Tolman-Oppenheimer-Volkov mass ($2.01 M_\odot$) is in line with predictions of realistic EOSs [43]. Shock heating will increase the pressure above its cold value at a given density given by Eq. (14). This is reflected by the thermal contribution to the pressure:

$$P_{\text{th}} = (\Gamma_{\text{th}} - 1)\rho\varepsilon_{\text{th}}, \quad (15)$$

where $\varepsilon_{\text{th}} = \varepsilon - \varepsilon_{\text{cold}}$, and $\varepsilon_{\text{cold}}$ is the specific internal energy consistent with the cold pressure:

$$\varepsilon_{\text{cold}}(\rho) = -\int P_{\text{cold}}(\rho) d\left(\frac{1}{\rho}\right). \quad (16)$$

In this paper, we take $\Gamma_{\text{th}} = 1.3$.

In low-density and/or highly magnetically dominated regions, we find that the inversion procedure for obtaining the primitive variables (ρ, P, v^i) from Eqs. (8)–(10)

sometimes returns an unphysical solution (i.e., a solution with negative pressure). In such grid zones, we apply the fix suggested by Font *et al.* [44], which consists of replacing the energy equation (10) by the cold EOS, $P = P_{\text{cold}}(\rho)$ when solving the system of equations. This substitution guarantees a positive pressure. In rare cases, this revised system also fails to give a solution and we repair the zone by averaging from nearby zones. (Averaging is not applied to the magnetic field, since this would introduce monopoles.) For a typical run with 500^2 resolution, we find that < 10 zones require this secondary fix on a given timestep.

The code used here has been tested in multiple relativistic MHD simulations, including MHD shocks, nonlinear MHD wave propagation, magnetized Bondi accretion, and MHD waves induced by linear gravitational waves [20]. We have also compared this code with the GRMHD code of Shibata and Sekiguchi [21] by performing simulations of the evolution of magnetized HMNSs [17, 19], and of magnetorotational collapse of stellar cores [45]. We obtain good agreement between these two independent codes.

B. Diagnostics

We keep track of the rest mass M_0 and angular momentum J on our grid by computing the following volume integrals:

$$M_0 = \int_V \rho_* d^3x, \quad (17)$$

$$J = \int_V \tilde{S}_\varphi d^3x. \quad (18)$$

Note that this formula for J is only valid in an axisymmetric spacetime [46]. The total rest mass M_0 is conserved (baryon number conservation), and angular momentum J is conserved in axisymmetry since gravitational radiation carries away no angular momentum. Our finite differencing scheme is designed to conserve M_0 and J as a numerical identity. This is possible since the continuity equation $\nabla_\mu(\rho u^\mu) = 0$ and momentum equation $\nabla_\mu T^\mu{}_i = 0$ can be written as

$$\partial_t \rho_* + \partial_j(\rho_* v^j) = 0, \quad (19)$$

$$\partial_t \tilde{S}_i + \partial_j(\alpha \sqrt{\gamma} T^j{}_i) = \frac{1}{2} \alpha \sqrt{\gamma} T^{\mu\nu} g_{\mu\nu,i}. \quad (20)$$

Taking the φ -component of the second equation, we obtain the equation for \tilde{S}_φ in axisymmetry:

$$\partial_t \tilde{S}_\varphi + \partial_j(\alpha \sqrt{\gamma} T^j{}_\varphi) = 0. \quad (21)$$

Note that both Eqs. (19) and (21) are written in conservative form with no source terms. This allows us to design a finite differencing scheme to conserve M_0 and J as a numerical identity.

In practice, the conservation of M_0 and J will not be exact for three reasons. Most significantly, outflows from the computational grid remove both rest mass and angular momentum. Secondly, as described in Section II A, the inversion from conserved to primitive variables requires on rare occasion a fix in which primitive variables are averaged from nearby cells. This averaging can affect the total rest mass and angular momentum. (In contrast, the fix suggested by Font *et al.*, which is much more commonly employed in our code, does not affect the rest mass and angular momentum since it does not change ρ_* and \tilde{S}_φ .) The third factor preventing strict conservation is the imposition of floor values for the rest mass density (see below). In particular, applying a density floor increases the total rest mass. We also find that the floor tends to increase the angular momentum as well. The rate of increase for these quantities can be judged from the early part of the simulation (before any outflow from the computational grid). Based on these rates, we find that the fractional increases in M_0 and J due to the floor is at most $\sim \text{few} \times 10^{-4}$ for the entire duration of the runs.

Soon after an apparent horizon forms, we excise the BH interior to continue the evolution [17, 39]. During the post-excision evolution, we compute the rest mass M_{out} and angular momentum J_{out} of the material outside the BH by computing integrals (17) and (18) over the volume outside the apparent horizon. This material includes the disk and corona, as well as any outbound material which may be on the grid. The irreducible mass M_{irr} of the BH is given by $M_{\text{irr}} = \sqrt{A/16\pi}$, where A is the surface area of the apparent horizon. Since J is conserved, we can compute the BH's angular momentum J_h by

$$J_h = J - J_{\text{out}}. \quad (22)$$

This would be exact only if the total angular momentum were strictly conserved. However, as mentioned above, strict conservation is broken by our atmosphere treatment, by our treatment of zones in which the primitive variable inversion fails, and because of outflows from the grid. We calculate that the angular momentum loss through the outer boundary is at most a few percent. Nevertheless, we assume J to be perfectly conserved after excision and hence use the value of J just before excision when computing J_h . The BH's mass M_h is then computed from the formula

$$M_h = \sqrt{M_{\text{irr}}^2 + (J_h/2M_{\text{irr}})^2}, \quad (23)$$

which is exact for a Kerr spacetime, and is in accord with the formula derived using the isolated and dynamical horizon formalism [47].

Shortly after BH excision (hundreds of M), the spacetime settles down to an approximately stationary state, and it is possible to define an (approximately) conserved energy:

$$E = - \int \alpha \sqrt{\gamma} T^t{}_t d^3x. \quad (24)$$

We can then define the fluxes of rest mass, energy, and angular momentum across any closed two-dimensional surface S in a time slice:

$$\dot{M}_0 = \oint_S \alpha \rho v^i d^2 \Sigma_i, \quad (25)$$

$$\dot{E} = - \oint_S \alpha T^i_t d^2 \Sigma_i, \quad (26)$$

$$\dot{J} = \oint_S \alpha T^i_\varphi d^2 \Sigma_i, \quad (27)$$

where

$$d^2 \Sigma_i = \frac{1}{2} \epsilon_{ijk} dx^j \wedge dx^k, \quad (28)$$

and $\epsilon_{ijk} = n_\mu \epsilon^{\mu}_{ijk}$ is the Levi-Civita tensor associated with the three-metric γ_{ij} . We use the above formulae for calculating fluxes through the apparent horizon when the apparent horizon has a general shape. However, the disk simulations in Section III are performed with a fixed Kerr background metric for which the horizon surface is spherical in our adopted coordinates. In such cases, the surface S is a sphere with radius r , and the flux expressions reduce to

$$\dot{M}_0(r) = \oint_{r=\text{const}} dA \rho_* v^r r^2 \quad (29)$$

$$\dot{E}(r) = - \oint_{r=\text{const}} dA \alpha \sqrt{\gamma} T^r_t, \quad (30)$$

$$\dot{J}(r) = \oint_{r=\text{const}} dA \alpha \sqrt{\gamma} T^r_\varphi, \quad (31)$$

where $dA = r^2 \sin \theta d\theta d\phi$.

To determine whether a fluid particle is unbound, we compute u_t . In a stationary spacetime, the value of u_t for a particle moving on a geodesic is conserved. If the particle is unbound, the radial velocity $v^r > 0$ and $-u_t = 1/\sqrt{1-v^2} > 1$ at infinity. Hence v^r and u_t provide an approximate criterion to determine whether a fluid element is unbound, provided that the fluid motion is predominantly ballistic and pressure and electromagnetic forces can be neglected. (We note that, in general, this condition is necessary but not sufficient even in the absence of external forces [48].)

III. MAGNETIZED DISK EVOLUTIONS

In order to verify the ability of our code to handle magnetized accretion flows in stationary spacetimes, we perform runs to compare with published results of McKinney and Gammie [29] (see also [49]) for the evolution of a magnetized Fishbone-Moncrief (FM) torus [30]. In particular, we consider the case referred to in [29] as the fiducial run. The spacetime metric corresponds to a fixed

Kerr BH with $M = 1$ in Kerr-Schild coordinates [29]:

$$\begin{aligned} ds^2 = & - \left(1 - \frac{2r}{\Sigma}\right) dt^2 + \left(\frac{4r}{\Sigma}\right) dr dt + \left(1 + \frac{2r}{\Sigma}\right) dr^2 \\ & + \Sigma d\theta^2 + \sin^2 \theta \left[\Sigma + a^2 \left(1 + \frac{2r}{\Sigma}\right) \sin^2 \theta \right] d\phi^2 \\ & - \left(\frac{4ar^2 \sin^2 \theta}{\Sigma}\right) dt d\phi \\ & - 2a \left(1 + \frac{2r}{\Sigma}\right) \sin^2 \theta dr d\phi, \end{aligned} \quad (32)$$

where $\Sigma = r^2 + a^2 \cos^2 \theta$ and the spin parameter is chosen as $a = 0.938$. (In this section, units with $M = 1$ will be assumed.) The BH is surrounded by a FM torus specified by $u^t u_\phi = 4.281$ and inner disk radius $r_{\text{in}} = 6$. The torus has an outer radius of 42 in the equatorial plane and the pressure maximum is located at $r = 12$. The FM solution provides the specific enthalpy distribution, from which the rest-mass density and pressure are derived assuming a cold polytropic EOS, $P = K \rho^\Gamma$, with $\Gamma = 4/3$. The constant K is chosen so that the maximum rest-mass density at $t = 0$ is unity. The torus is evolved assuming the equation of state $P = (\Gamma - 1)\rho\epsilon$ (again with $\Gamma = 4/3$), in order to account for entropy generation in shocks.

In the absence of magnetic fields and viscosity, the torus is in equilibrium. However, following [29], we add a small poloidal magnetic field by specifying the azimuthal component of the magnetic vector potential:

$$A_\varphi \propto \max[(\rho - \rho_{\text{cut}}), 0], \quad (33)$$

where the cutoff density ρ_{cut} is chosen as $0.2\rho_{\text{max}} = 0.2$. This form of A_φ results in magnetic field loops confined within the torus. The proportionality constant determines the strength of the magnetic field and is chosen so that $\max(P_{\text{mag}})/\max(P) = 0.01$. Thus, the dynamical equilibrium of the torus is only slightly perturbed by the addition of the magnetic field.

We evolve these initial data assuming axial and equatorial symmetry and using cylindrical coordinates (ϖ, z) . In addition, we introduce a logarithmic radial coordinate transformation in order to concentrate zones near the BH event horizon. In particular, we take

$$r = e^{(\bar{r}-r_0)}, \quad r_0 = 0.2, \quad (34)$$

and then $\bar{\varpi} = (\bar{r}/r)\varpi$ and $\bar{z} = (\bar{r}/r)z$. We perform three runs having 200^2 , 320^2 , and 400^2 zones, with uniform resolution in $(\bar{\varpi}, \bar{z})$ and with the outer boundaries held fixed at $\bar{\varpi}_{\text{max}} = \bar{z}_{\text{max}} = 4.0$. The resulting grid is non-uniform in ϖ and z , and the outer boundary in the (ϖ, z) -plane is not square. At its point of closest approach to the origin in the (ϖ, z) -plane, the outer boundary is located at a radius $r = 44.7$. In contrast to our distorted rectangular grid, McKinney and Gammie [29] employ spherical polar coordinates with a logarithmic radius and θ -zones concentrated toward the disk plane. As in many hydrodynamic simulations in astrophysics, we add a tenuous

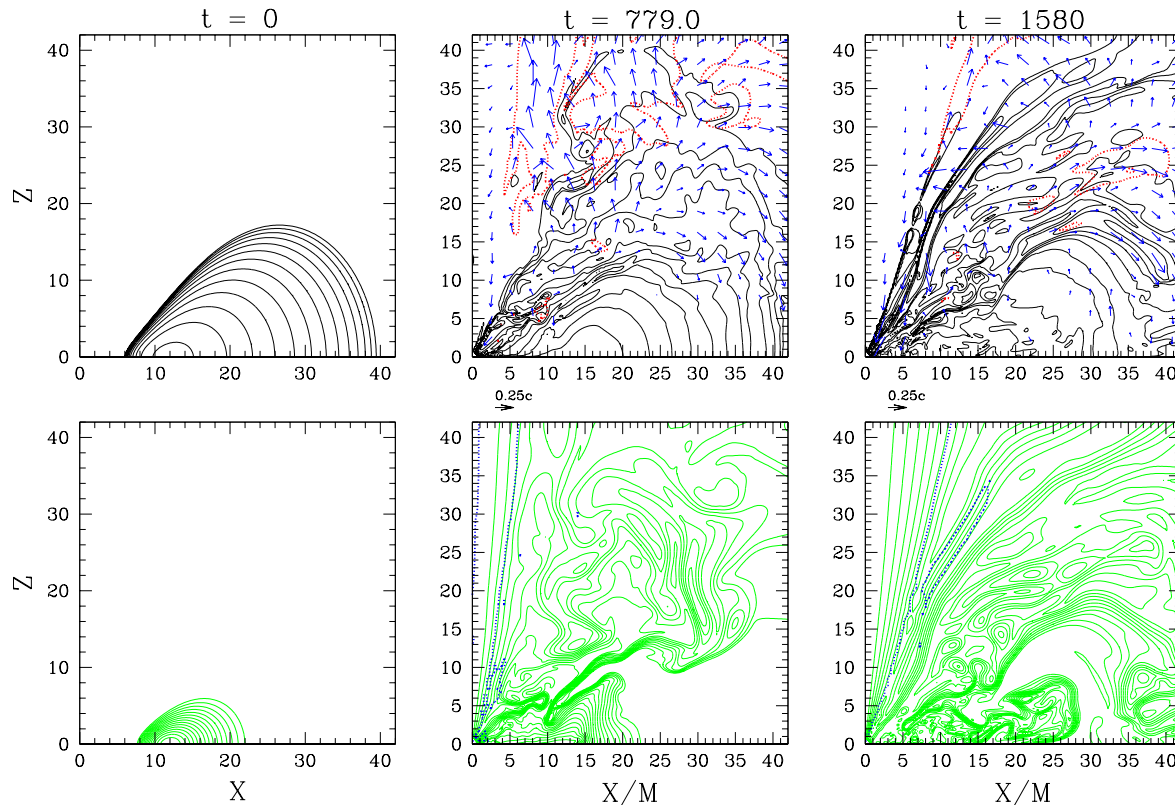


FIG. 1: Panels in the first row show density contours (solid black lines) and velocity vectors at selected times during the evolution of the magnetized FM torus. The dotted (red) contour lines enclose regions with unbound outflows (having $-u_t > 1$ and positive radial velocity). The second row shows the poloidal magnetic field structure at the corresponding times. The dotted blue contours correspond to $\beta = P/P_{\text{mag}} = 0.01$ and thus enclose magnetically dominated regions (such as the funnel region near the polar axis in the last two snapshots). In this and all subsequent density contour plots, levels are defined by $\rho/\rho_{\text{max}} = 10^{-0.3i-0.09}$ ($i = 0-12$). Likewise, for all plots of magnetic field lines, the field lines are drawn as contours of A_φ according to $A_\varphi = A_{\varphi,\text{min}} + (A_{\varphi,\text{max}} - A_{\varphi,\text{min}})i/20$ ($i = 1-19$), where $A_{\varphi,\text{max}}$ and $A_{\varphi,\text{min}}$ are the maximum and minimum values of A_φ .

TABLE I: Resolution Study

Resolution	$-\dot{M}_0^{\text{a}}$	\dot{E}/M_0	\dot{J}/M_0	$\lambda_{\text{max}}/\Delta^{\text{b}}$
200^2	0.29	0.87	1.66	6
320^2	0.36	0.82	1.45	10
400^2	0.37	0.82	1.35	12

^a The averaging period for the values of $-\dot{M}_0$, \dot{E}/M_0 , and \dot{J}/M_0 in this table is $500 < t < 1000$. (Here, we assume units with BH mass $M = 1$.)

^b The ratio of the typical MRI wavelength at $t = 0$ to the grid resolution in the neighborhood of the (gas) pressure maximum.

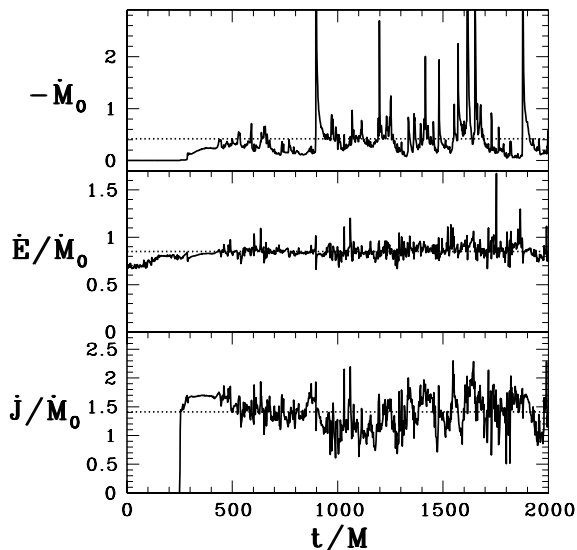


FIG. 2: Upper panel shows the rest-mass accretion rate (solid line), along with its time-averaged value 0.42 (dotted line). (Here, time averages are performed over the period $500 < t < 2000$.) The middle (lower) panel shows the ratio of the accretion rate of total energy (angular momentum) to the rest mass accretion rate. The time averaged values (dotted lines) are $\dot{E}/\dot{M}_0 = 0.85$ and $\dot{J}/\dot{M}_0 = 1.41$. (Here, we assume units with BH mass $M = 1$.)

“atmosphere” that covers the computational grid outside the star. Following [29], this is done by imposing floors on both the rest-mass density and pressure as follows: $\rho_{\text{atm}} = 10^{-4}r^{-3/2}$ and $P_{\text{atm}} = 3.3 \times 10^{-7}r^{-5/2}$.

We first discuss the general features of the evolution. Figure 1 shows snapshots of isodensity contours and velocity vectors (in the top row), and of the poloidal magnetic field lines (in the bottom row, drawn as contours of constant A_φ). The snapshots at $t = 0$ show the initial density distribution of the torus and the loops of magnetic field confined within it. The MRI and magnetic braking cause angular momentum transport in the disk, leading to accretion onto the central BH and ejection of some material. Magnetic field lines carried into this central region are stretched upward by outgoing material, leading to the collimation of field lines in the region of the spin axis. This collimated structure (first seen in the snapshots at $t = 779$ in Fig. 1) persists through the rest of the simulation. The panels in Fig. 1 showing the magnetic field lines also have dotted contours corresponding to $\beta = P/P_{\text{mag}} = 10^{-2}$. These contours enclose the collimated magnetic field lines, showing that this funnel region is strongly magnetically dominated.

The MRI-driven turbulence causes the magnetic field remaining in the disk to become highly tangled. The violent motions of the disk lead to the ejection of material, especially near the outer edge of the collimated magnetic field region (i.e., the funnel wall, or funnel-corona interface as discussed in [29]). In the top row of panels, the

dotted contours surround regions which have $-u_t > 1$ and positive radial velocity, roughly corresponding to regions of outflow. Such regions can be seen just outside the magnetically dominated funnel in the last two sets of snapshots in Fig. 1.

Figure 2 shows the mass accretion rate \dot{M}_0 as a function of time for the 400^2 case, along with the ratios \dot{E}/\dot{M}_0 , and \dot{J}/\dot{M}_0 (where \dot{E} and \dot{J} are the total energy and angular momentum fluxes through the horizon). These quantities are calculated as integrals over the horizon surface using Eqs. (29)-(31). (We exclude from these integrals those zones which may have been affected by a failed primitive variable inversion. These failures tend to occur in the small region near the polar axis which is highly magnetically dominated. In particular, by examining these failures at several times, we find that $> 99\%$ of the failures occur in regions where $\beta = P/P_{\text{mag}} < 10^{-4}$, while $> 70\%$ of the failures occur for $\beta < 10^{-5}$.) The time averaged values (for the period $500 < t < 2000$) are $-\dot{M}_0 = 0.42$, $\dot{E}/\dot{M}_0 = 0.85$, and $\dot{J}/\dot{M}_0 = 1.41$ and are shown as dotted lines in Fig. 2. These are in good agreement with the values given by McKinney and Gammie [29] for the same averaging period: $-\dot{M}_0 = 0.35$, $\dot{E}/\dot{M}_0 = 0.87$, and $\dot{J}/\dot{M}_0 = 1.46$. Finally, we show in Table I that these characteristics of the accretion flow are consistent for all three resolutions considered. In addition, the table gives the ratio of the typical unstable wavelength of the MRI to the spatial resolution. As an estimate of the typical MRI wavelength at $t = 0$, we take a typical value of

$$\lambda_{\text{max}} \simeq \frac{8\pi v_A^z}{\sqrt{15}\Omega} \quad (35)$$

in the equatorial plane, where $\mathbf{v}_A = \mathbf{B}/\sqrt{4\pi\rho}$ is the (Newtonian) Alfvén velocity and $\Omega = v^\varphi$ is the angular velocity [28, 45]. (This expression is exact for Newtonian flows with a Keplerian angular velocity profile.) Our highest resolution (400^2) thus gives ~ 12 points across the MRI wavelength. We expect that the MRI is fairly well resolved for the two higher resolution runs (320^2 and 400^2) and perhaps marginally resolved in the 200^2 run. The rough quantitative agreement between our results and those of [29] is quite reasonable given the very different grid structures employed by the two codes and gives us confidence in the ability of our code to handle complex accretion flows.

IV. RESULTS FOR HMNS EVOLUTION

We now turn to magnetized HMNS collapse and the remnant accretion disk evolution. We describe the initial data models and the three evolution cases in Section IV A. We then describe the results and implications for jet formation from HMNS collapse.

A. Initial Data

The evolution cases described below employ the two HMNS models referred to in [19] as stars A and C. (For the sake of consistency, those labels will be retained in the present paper.)

Since star A is constructed using a $\Gamma = 2$ polytropic EOS, $P = K\rho^\Gamma$, this model may be scaled to any desired physical mass by adjusting the value of K [50]. In contrast, star C is constructed with the more realistic cold hybrid EOS given in Eq. (14). This hybrid EOS introduces a physical density scale, and star C thus does not have the scale freedom enjoyed by star A. For definiteness and ease of comparison between the evolution cases, we fix the value of the polytropic constant for star A in the discussion below to $K = 1.37 \times 10^5 \text{g}^{-1} \text{cm}^5 \text{s}^{-2}$. This value was chosen so that stars A and C have the same rest mass ($M_0 = 2.95 M_\odot$). With this choice, Table II lists some properties of these stars. We note that the rest masses of stars A and C exceed the supramassive limits (i.e., the mass limits for rigid rotation) by 46% and 14%, respectively. These stars rotate very rapidly and are highly flattened due to centrifugal force. We also note that the parameters of star C are chosen in order to mimic the HMNSs formed through binary NS mergers with realistic EOSs in [11].

As in previous papers (e.g, [4, 5, 19, 20, 50]), we choose the initial rotation law $u^t u_\varphi = A^2(\Omega_c - \Omega)$, where u^μ is the four-velocity, Ω_c is the angular velocity along the rotational axis, and $\Omega \equiv u^\varphi/u^t$ is the angular velocity. In the Newtonian limit, this differential rotation law becomes

$$\Omega = \frac{\Omega_c}{1 + \frac{\varpi^2}{A^2}}. \quad (36)$$

The constant A has units of length and determines the steepness of the differential rotation. In this paper, A is set equal to the coordinate equatorial radius R_{eq} for star A and to $0.8R_{\text{eq}}$ for star C. The corresponding values of $\Omega_{\text{eq}}/\Omega_c$ are shown in Table II (where Ω_{eq} is the angular velocity at the equatorial surface).

We must also specify initial conditions for the magnetic field. We choose to add a weak poloidal magnetic field to the equilibrium model by introducing a vector potential taking one of the following forms:

$$A_\varphi = A_b \varpi^2 \max(P - P_{\text{cut}}, 0), \quad (37)$$

or

$$A_\varphi = A_b \varpi^2 \max(\rho^{3/2} - \rho_{\text{cut}}^{3/2}, 0), \quad (38)$$

with cutoffs $\rho_{\text{cut}} = 0.04\rho_{\text{max}}$ and $P_{\text{cut}} = 0.04P_{\text{max}}$. [Note that our previous study [19] uses the form in Eq. (37).] As with Eq. (33), these prescriptions result in poloidal loops of magnetic field confined within the stars. Since the physically realistic magnetic field configuration is unknown, we adopt this simple prescription as a first step.

This is numerically convenient since confining the initial magnetic field to the high density regions allows us to avoid strongly magnetically dominated regions in the initial data. The proportionality constant A_b determines the initial strength of the magnetic field. We characterize the strength of the initial magnetic field by $C \equiv \max(b^2/P)$. We choose A_b such that $C \sim 10^{-3} - 10^{-2}$. We have verified that such small initial magnetic fields introduce negligible violations of the Hamiltonian and momentum constraints in the initial data. For example, without the magnetic field, the normalized Hamiltonian constraint violation due to discretization error is 0.57% for Star C. For the strongest magnetic field case, C2 (see below), adding the magnetic field increases the constraint violation by a fraction 1.8×10^{-5} .

We discuss results of three evolutions, one with star A, and two with star C (labeled C1 and C2). Case A is a continuation of the star A run in [19] starting from the point of excision ($t = 2570M = 66.9P_c$). In the present paper, we evolve the system through the post-excision phase and then, for an extended period, in the Cowling approximation. Thus, we consider the longer-timescale behavior of the same model presented in [19]. For case A, the magnetic field at $t = 0$ takes the form given in Eq. (37), with $C = 2.5 \times 10^{-3}$, giving $B_{\text{max}}^x = 9.63 \times 10^{15}$ G. This run uses a constant atmosphere floor density $\rho_{\text{atm}} = 10^{-7}\rho_{\text{max}}(t = 0) = 4.5 \times 10^7 \text{g/cm}^2$. We also impose a pressure floor given by $P_{\text{atm}} = 5 \times 10^{-15}P_{\text{max}}$. This pressure floor is quite small because it is determined by taking half of the cold polytropic pressure at the atmosphere density, and the EOS has $\Gamma = 2$. In practice, this pressure floor is rarely invoked. These values for the pressure and density floors are chosen as in [19] since this run is a continuation of the earlier run.

The two runs involving star C differ only in their magnetic field configurations. Case C1 has an initial magnetic field of the form given by Eq. (37), and $C = 8.3 \times 10^{-3}$ ($B_{\text{max}}^x = 1.81 \times 10^{16}$ G). Case C2, on the other hand, uses the form in Eq. (38), which has the effect of shifting the initial distribution of magnetic field energy toward the outer layers of the star. Figure 3 shows the initial density contours and the magnetic field lines obtained from the two prescriptions for A_φ . We choose the coefficient A_b for case C2 such that $C = 9.1 \times 10^{-2}$ ($B_{\text{max}}^x = 1.84 \times 10^{16}$ G). Though this value of C is larger than our previous choices, we note that the *average* value of b^2/P is 5×10^{-3} . Thus, the overall perturbation to the star is still small, and we do not observe any artifacts from it during the evolution. Both cases C1 and C2 use an atmosphere prescription inspired by the disk evolutions in [29], in which floors on pressure and density fall off with radius according to: $\rho_{\text{atm}} = 10^{-7}\rho_{\text{max}}(t = 0)r^{-3/2}$ and $P_{\text{atm}} = 1.37 \times 10^{-4}P_{\text{max}}(t = 0)r^{-5/2}$. This prescription for the pressure floor gives an atmosphere which is significantly hotter than the cold pressure corresponding to ρ_{atm} determined by the hybrid EOS. We find that using a hot atmosphere with this EOS leads to fewer failures of the primitive variable inversion. The radial dependen-

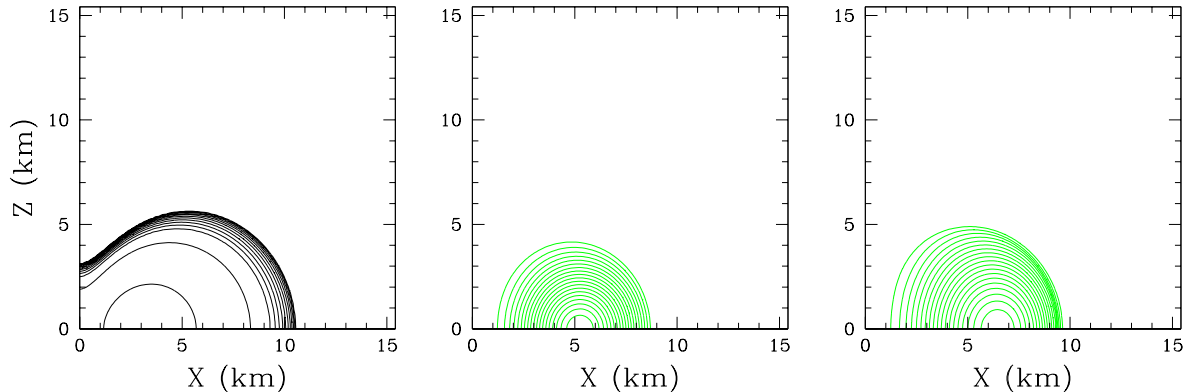


FIG. 3: The left panel shows density contour lines for star C at $t = 0$. The middle and right panels show initial magnetic field lines for cases C1 and C2, respectively. Contour lines have the same meaning as in Fig. 1.

TABLE II: Initial Models

Model	$M(M_{\odot})$	$M_0(M_{\odot})$	$R_{\text{eq}}/M^{\text{a}}$	J/M^2	$T_{\text{rot}}/ W ^{\text{b}}$	$\Omega_{\text{eq}}/\Omega_c^{\text{c}}$	P_c/M^{d}
A	2.71	2.95	4.48	1.0	0.249	0.33	38.4
C	2.64	2.95	2.75	0.82	0.241	0.185	15.5

^a The equatorial coordinate radius R_{eq} normalized by the Arnowitt-Deser-Misner (ADM) mass.

^b The ratio of the rotational kinetic energy to the gravitational binding energy.

^c The ratio of the angular velocity at the equator to the central angular velocity.

^d The initial central rotation period P_c .

cies are *ad hoc*, but the purpose of the atmosphere to stabilize the evolution without significantly affecting the physical outcome. Allowing the density floor to decrease with radius may further reduce the impact of the atmosphere on the physical behavior [51]. Whereas case A begins with the post-excision phase after the HMNS has collapsed, cases C1 and C2 are evolved from $t = 0$.

All three cases are evolved with 500^2 uniform spatial resolution in (ϖ, z) . In case A, the outer boundaries are located at $4.5R_{\text{eq}} = 20.1M = 80.3$ km. For the runs with star C, the outer boundaries are placed at $5R_{\text{eq}} = 13.7M = 53.6$ km.

B. Results for Star A

The presence of the small seed magnetic field in star A renders the star secularly unstable. Magnetic winding and the MRI transport angular momentum outward, leading to contraction of the core and expansion of the outer layers. The core eventually becomes radially unstable to collapse, which occurs at $t \approx 2535M = 66P_c$. This leads to the formation of a BH surrounded by a magnetized accretion disk. (For a detailed discussion of the pre-collapse and early disk evolution of this model,

see [19].)

Our code quickly loses accuracy after the formation of the BH due to grid stretching on the BH throat. In order to prevent this, we excise the interior region surrounding the singularity from the grid at $t = t_{\text{ex}} = 2570M$. Excision may not be necessary. Alternative methods have been suggested to handle the black hole spacetime in the presence of matter [52, 53]. Whether this technique would be effective for the simulations described here deserves further study. For the present, we will employ the standard excision technique. We note that, during the pre-excision evolution, the L2 norms of the Hamiltonian and momentum constraints (as defined in [19]) are satisfied to better than 1%. During the excision evolution, the maximum values of the constraints are given by $(\mathcal{H}, \mathcal{M}^x, \mathcal{M}^y, \mathcal{M}^z) = (0.5\%, 0.5\%, 3\%, 0.75\%)$.

As discussed in [19], we are only able to perform the post-excision evolution accurately for $\sim 400M$. In order to consider the disk behavior on longer timescales, we freeze the spacetime metric after the BH has settled down to a quasi-stationary state. We then evolve the MHD equations in this fixed spacetime (i.e., the Cowling approximation). We start the Cowling phase at $t = 2997M$. The duration of the post-excision phase (with live BSSN evolution) is thus $427M$. (We note that the accretion

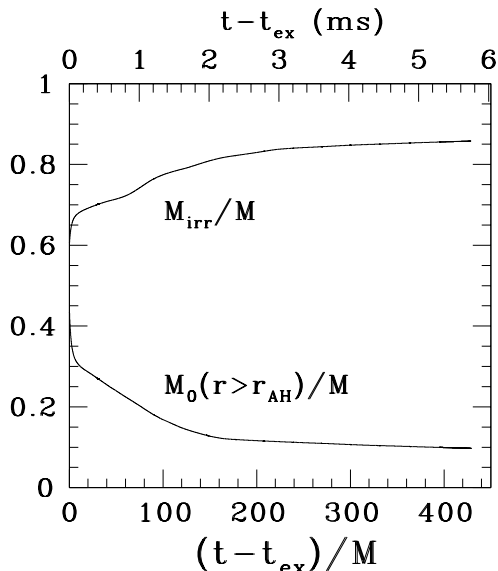


FIG. 4: Irreducible mass (M_{irr}) and the rest mass remaining outside the apparent horizon for case A, normalized by the ADM mass (M) at $t = 0$. Time is given in units of M (bottom axis) and in units of ms (top axis). By the end of the post-excision run, which lasts $427M$, the BH has settled to a quasi-stationary state.

flow, which has little effect on the spacetime metric, is strongly time dependent when the Cowling approximation is first imposed. The evolution of the disk itself is thus not yet quasi-stationary.) The Cowling phase of the evolution lasts for a further $1912M$. At the beginning of the Cowling phase, the rotation period near the middle of the disk is $\sim 164M$. Thus the post-excision and Cowling phases encompass ~ 14 rotation periods of the disk. We note that the change in the disk mass during the Cowling phase is about 3% of the total rest mass. The Cowling approximation does not take this change into account, but the approximation should be fairly accurate since the self-gravity of the disk is estimated to affect the dynamics by $\sim (M_{\text{disk}}/M)$, and the error is thus $\sim \Delta M_{\text{disk}}/M \sim 3\%$ (where ΔM_{disk} is the change in the disk mass during the Cowling phase).

Figure 4 shows the evolution of the irreducible mass and the rest mass remaining outside the horizon during the post-excision phase. Following a period of rapid accretion (representing the final stages of collapse), the accretion slows down to a quasi-stationary rate. This transition occurs at $t - t_{\text{ex}} \sim 170M$. We can estimate the BH mass M_h and angular momentum J_h at this time [see Eqs. (22) and (23)], and we find that $M_h = 0.91M$ and $J_h/M_h^2 = 0.79$. Figure 5 shows snapshots during the post-excision and Cowling phases. We find no evidence for significant unbound outflows in this case (aside from a transient which can be seen in the first set of panels). Accretion from the disk takes place primarily near the equatorial plane, and very little material is churned up from the disk into a corona. The

disk thus reaches an essentially quasi-stationary state. To check that the lack of outflows in this case is not caused by our constant density floor, we also performed this evolution with floors which fall off with radius. In particular, we set $\rho_{\text{atm}} = 10^{-7}\rho_{\text{max}}(t = 0)r^{-3/2}$ and $P_{\text{atm}} = 10^{-14}P_{\text{max}}(t = 0)r^{-5/2}$. However, this did not make any qualitative difference in the outcome, and no significant outflows were observed.

Finally, we plot accretion rates through the apparent horizon during the Cowling phase in Figure 6. Averaging \dot{E} , \dot{J} , and \dot{M}_0 individually over the duration of the Cowling run, we find the ratios $\dot{E}/\dot{M}_0 = 0.81$ and $\dot{J}/(M_h\dot{M}_0) = 2.2$. These are in rough agreement with Table 2 of [29], which gives results for disk evolutions with varying BH spin. Though their table does not give results for a BH with the specific spin parameter $J_h/M_h^2 = 0.8$, (which is the estimate for the BH in case A), the nearby table entries suggest $\dot{E}/\dot{M}_0 \sim 0.9$ and $\dot{J}/(M_h\dot{M}_0) \sim 2$. (Note that $M_h = 1$ in [29].) Roughly speaking, the $\dot{J}/(M_h\dot{M}_0)$ ratio increases as the BH spin decreases because the innermost stable circular orbit (from which material plunges into the BH) moves outward in radius as the spin decreases. This explains why accretion onto star A gives a higher value for $\dot{J}/(M_h\dot{M}_0)$ than the disk simulation in Section III, for which the BH has higher spin $J_h/M_h^2 = 0.938$.

C. Results for Star C

We now describe the evolution of the hybrid EOS models C1 and C2. The behavior of both models up to the collapse and BH formation is represented in Fig. 7. Secular MHD effects result in initially linear growth of $|B^y|_{\text{max}}$ due to magnetic winding and sudden spurts of exponential growth of $|B^x|_{\text{max}}$ due to the MRI (for a detailed discussion, see [19]). These MHD effects lead to collapse much later in the case of C2 than in the case of C1. This is due to the different magnetic field distributions in the two models. Since A_φ is proportional to $\rho^{3/2}$ for C2, the magnetic field is stronger in the outer regions and weaker in the interior as compared with C1 (see Fig. 3). However, collapse is triggered by transporting angular momentum from the interior to the exterior. Since the interior magnetic field is weaker for case C2, this process takes longer and the collapse is delayed. Both models eventually form BHs surrounded by magnetized accretion disks. Constraint violations remain less than 2% during the pre-excision evolution for both of these models.

For case C1, collapse occurs at $t \sim 939M = 61P_c$. We excise the singularity at $t = t_{\text{ex}} = 941M$ and freeze the spacetime metric at $t = 1221M$. Thus, the live BSSN evolution with excision lasts for $280M$, and the maximum constraint violations during the post-excision phase are $(\mathcal{H}, \mathcal{M}^x, \mathcal{M}^y, \mathcal{M}^z) = (0.5\%, 4\%, 8\%, 3\%)$. We evolve the system in the Cowling approximation for a further $1876M$ after the post-excision evolution ends. At the beginning of the Cowling phase, the rotation period

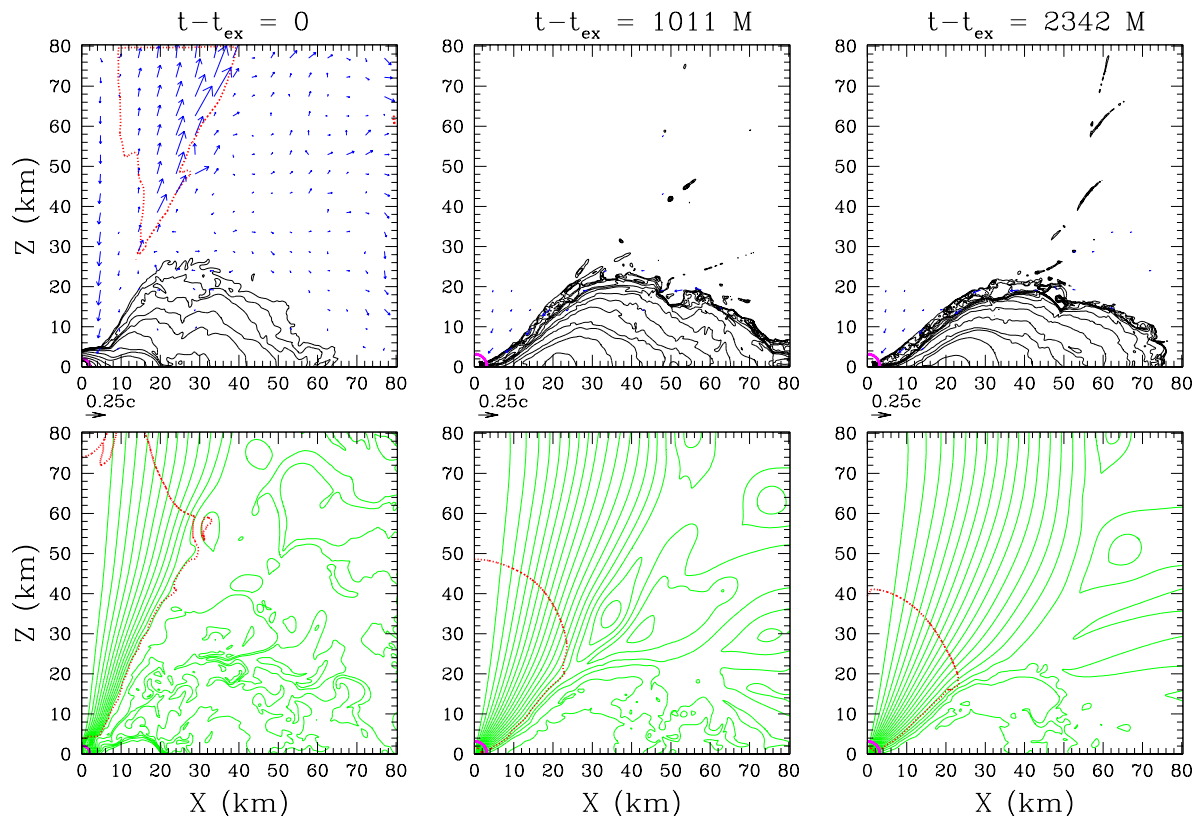


FIG. 5: Post-excision and Cowling evolution of star A at selected times. The upper panels show density contours and velocity vectors and the lower panels show the poloidal magnetic field lines. The dotted (red) contour lines enclose regions with unbound outflows (upper panels) and regions with $b^2/\rho \geq 1$ (lower panels). The heavy magenta circle centered on the origin marks the location of the apparent horizon.

midway through the disk is $\sim 148M$, and thus the post-excision and Cowling phases together cover roughly 16 periods of the disk. Following the collapse, the phase of extremely rapid accretion transitions to a slower rate at a time $t - t_{\text{ex}} \sim 46M$. Estimating the BH mass and angular momentum at this time [following Eqs. (22) and (23)] gives $M_h = 0.93M$ and $J_h/M_h^2 = 0.71$. We note that the collapse time found here differs from the collapse time of $511M = 33P_c$ given for the corresponding model in [19]. This is likely due to the sensitivity of the system as it becomes marginally stable.

Snapshots of the evolution during the post-excision and Cowling phases are shown in Fig. 8. (Contours showing $-u_t = 1$ are left out of this figure for the sake of clarity, but see Fig. 9.) Several features of the evolution are immediately apparent. As before, a low-density funnel region containing a collimated magnetic field has formed along the axis and persists through the evolution. In the first three snapshots (post-excision and early Cowling phases), there is a considerable amount of material and magnetic field in a low density corona above the disk. As material in this corona falls toward the central BH, the attached magnetic field lines make contact with the collimated magnetic field and reconnect. Material at-

tached to the reconnected field line is then driven outward along the corona-funnel boundary by magnetic buoyancy. (This process is easiest to see in an animation, but can also be seen, for example, in the $t - t_{\text{ex}} = 280M$ snapshot of Figure 9 at $x \sim 20$ km and $z \sim 47$ km. There, an unbound blob of material attached to reconnected field lines moves toward the edge of the grid.) Though we have not included a physical model for resistivity in our code, this reconnection is ubiquitous in HRSC codes for ideal MHD and physical reconnection is expected to operate in systems with MHD turbulence such as this (see, e.g. [54]).

This process leads to an intermittent outflow along the corona-funnel wall boundary. The outflow is mildly relativistic, with typical Lorentz factors ranging between 1.2 and 1.5. In Fig. 10, we plot the approximate maximum asymptotic Lorentz factors associated with the outflow for both the excision and Cowling phases. The time-averaged value for the maximum is 1.2. We find that this outflow dies down as the Cowling evolution proceeds (see Fig. 13 below). As may be seen in the last three panels of Fig. 8, the corona gradually empties of matter and magnetic fields, leaving a quasi-stationary disk surrounding the BH. Without the turbulent driving of reconnection

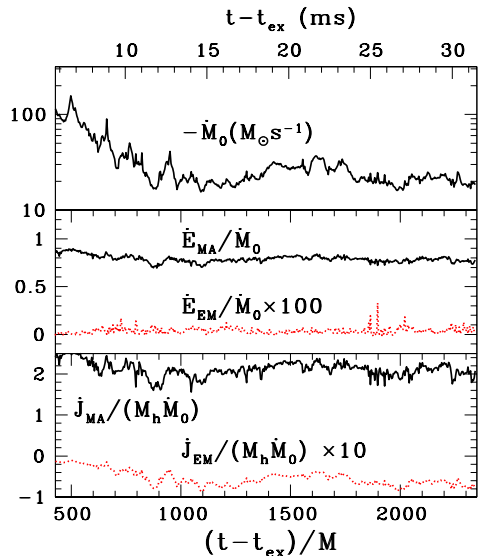


FIG. 6: Fluxes through the apparent horizon during the Cowling evolution of star A. The upper panel shows the negative of the rest mass flux in units of solar masses per second (where $\dot{M}_0 < 0$ indicates flow *into* the horizon). The middle panel shows separately the matter and electromagnetic contributions to the total energy flux (\dot{E}_{MA} and \dot{E}_{EM} respectively), normalized by \dot{M}_0 . Note that the electromagnetic contribution has been multiplied by a factor of 100. The lower panel shows the electromagnetic and matter contributions to the angular momentum flux through the horizon (\dot{J}_{MA} and \dot{J}_{EM} respectively), normalized by $M_h \dot{M}_0$ to yield a non-dimensional ratio. The electromagnetic contribution has been multiplied by a factor of 10.

across the funnel-corona boundary, the outflow largely ceases. In addition, the draining of pressure in the corona allows the magnetic field in the funnel to expand outward, as may be clearly seen in the last panel of Fig. 8. The corona thus plays a role in confining the magnetically dominated funnel region, as found by McKinney [34]. It is possible that the corona would be sustained in a 3D evolution, for which the turbulent magnetic field growth is not limited by the anti-dynamo theorem [55]. With our current computational resources, it would not be feasible to perform this run in 3D with high enough resolution to capture the MRI.

Case C2 undergoes collapse at $t \sim 3003M = 194P_c$, and we excise the singularity at $t = t_{ex} = 3008M$. The Cowling phase begins at $t = 3251M$, giving a live BSSN post-excision run of duration $243M$. During the post-excision phase, the maximum normalized Hamiltonian and momentum constraints are $(\mathcal{H}, \mathcal{M}^x, \mathcal{M}^y, \mathcal{M}^z) = (0.4\%, 1, 5\%, 13\%, 3\%)$. The Cowling phase continues for an additional $1282M$ beyond the end of the post-excision run. (A longer Cowling evolution is not necessary since the matter reaches an essentially quasi-stationary state.) The rotation period midway through the disk at the beginning of the Cowling phase is $\sim 67M$, and thus the

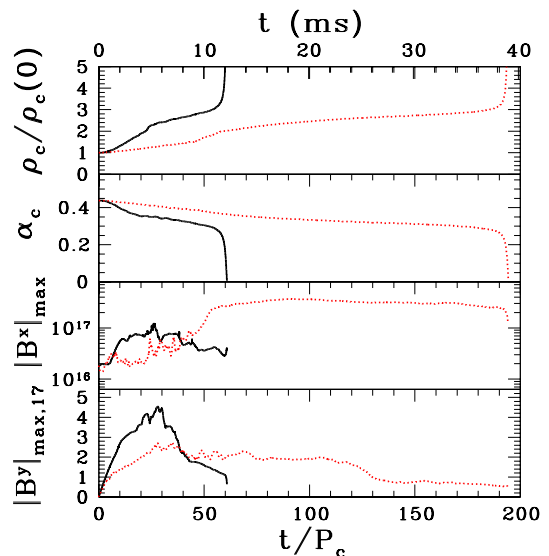


FIG. 7: Pre-excision evolution for cases C1 (solid black line) and C2 (red dashed line). From top to bottom, the quantities plotted are: (i) the central rest-mass density normalized by its initial value, (ii) the central lapse, (iii) the maximum value of $|B^x|$ in units of gauss (G), and (iv) the maximum value of $|B^y|$ in units of 10^{17} G. Collapse occurs in case C1 much earlier than in case C2.

post-excision and Cowling phases together cover roughly 22 periods of the disk. (Note that the disk in this case is considerably more compact than that of C1.) Following the collapse, the transition from extremely rapid to slower accretion occurs at $t \sim 3055M = 197P_c$. Estimating the BH mass and angular momentum at this time gives $M_h = 0.97M$ and $J_h/M_h^2 = 0.77$.

Selected snapshots from the post-excision and Cowling phases of evolution of case C2 are shown in Fig. 11. In contrast to case C1, no significant outflows are seen for this case (except for a transient seen in the first panel). The corona region contains much less material and magnetic field at the beginning of the post-excision evolution than in case C2. This allows the funnel region to expand, and it rapidly assumes the structure seen in the last two sets of panels. The relative absence of material in the corona is likely due to the much more rapid accretion following collapse. This can be seen in Fig. 12, which shows the evolution of the irreducible mass and the mass remaining outside the horizon in the two star C cases. For C2, M_{out} drops very rapidly after excision (solid black line), while the accretion takes place over a longer period of time for case C1. This may be understood from the difference in initial magnetic field configurations. For C2, more of the star's mass is initially threaded by magnetic field lines. Since the magnetic field remaining in the disk after collapse is thus stronger for case C2, the angular momentum transport is more efficient and the accretion is more rapid.

The comparative lack of outflows in C2 can also be

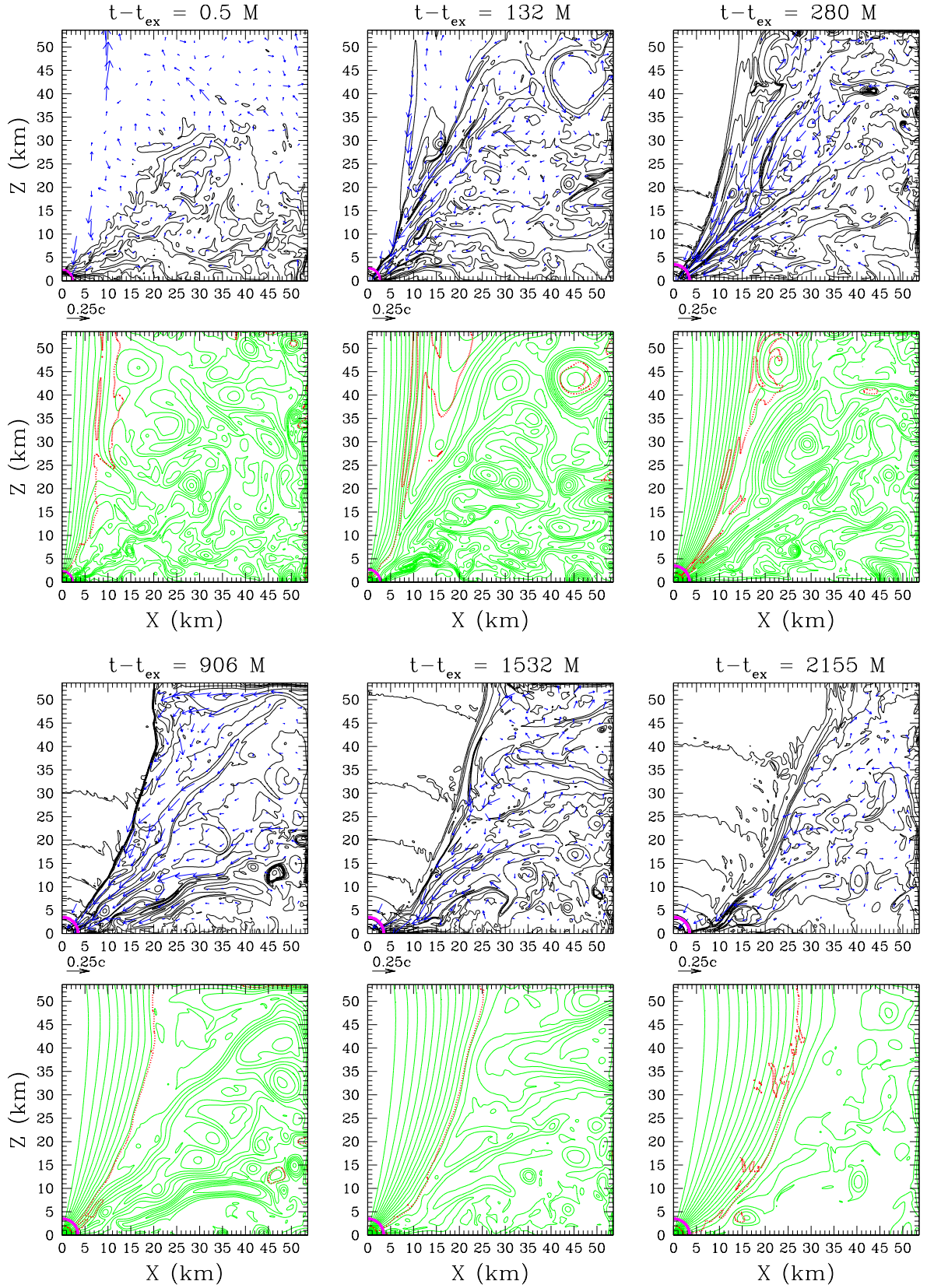


FIG. 8: Post-excision and Cowling evolution phases of case C1, shown at selected times. The meanings of the lines are the same as in Fig 5, except that the $u_t = -1$ contours have been left out for the sake of clarity. The first and last sets of panels represent the beginning of the post-excision phase and the end of the simulation, respectively. The panel at $t-t_{\text{ex}} = 280M$ marks the beginning of the Cowling phase.

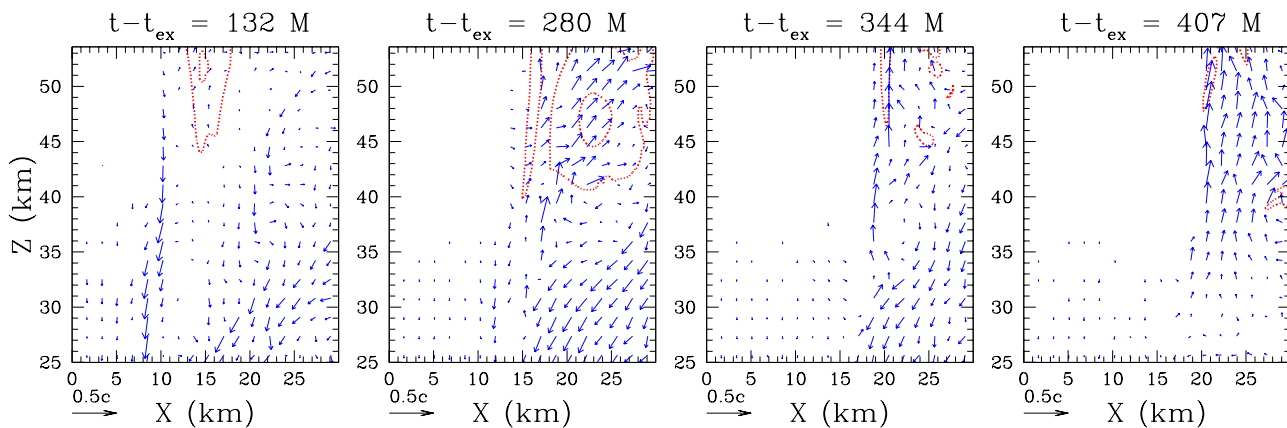


FIG. 9: Dotted contours demarcating regions with $-u_t \geq 1$, and velocity vectors. Note that the domain in these plots corresponds to the upper left-hand corner of the domain shown in Fig. 8. These snapshots demonstrate the funnel wall outflow, and the first two times correspond to the second and third sets of panels in Fig. 8

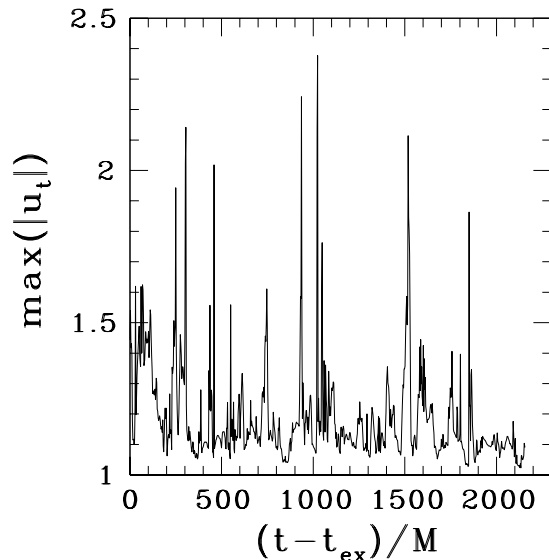


FIG. 10: The maximum value of $|u_t|$ on the grid as a function of time since excision for C1. This maximum is restricted to regions with outwardly directed velocity and with density greater than 10 times the atmosphere floor level. This quantity gives an approximation to the maximum asymptotic Lorentz factor associated with the outflow. Hence, the intermittent outflow is mildly relativistic.

seen by comparing the rest mass fluxes through an outer spherical shell for cases C1 and C2. This is shown in Fig. 13, where the shell is placed at $r = 12.2M = 47.7$ km. This spherical shell cuts through the disk as well as the outflow region, and thus there is a negative contribution from the inflow at lower latitudes. This overall inflow behavior is punctuated by intermittent outflows in the C1 case, while the flux through this shell is much smaller in the C2 case. These intermittent outflows eventually die down as the turbulence driving the outflow

decays. As in case C2, the lack of outflows in case A is likely caused by the lack of fluid and magnetic field in the corona region, which is in turn due to the EOS. Star A uses a $\Gamma = 2$ law for all density regimes, whereas the star C EOS corresponds to $\Gamma = 1.3$ in the low density regions of interest in the disk and corona. The softer EOS for star C allows more efficient shock heating, which aids the ejection of material into the corona. This interpretation is corroborated by the results of Mignone and McKinney [56], who found that using $\Gamma = 4/3$ in FM torus simulations leads to more vigorous turbulence and a thicker corona than the same case with $\Gamma = 5/3$.

Finally we plot the various flux quantities for the two star C cases in Figures 14 and 15. The upper panels show the rest mass flux through the horizon, which again demonstrates that, for case C2, the accretion is very rapid at first but then decays rapidly. The decrease in accretion rate for C1, on the other hand, is more gradual. Averaging over the duration of the Cowling evolution, we find that $\dot{E}/\dot{M}_0 = 0.90$ and $\dot{J}/(M_h \dot{M}_0) = 2.2$ for case C1. For case C2, these values are instead 0.90 and 2.7. Cases C1 and C2 produce BHs with $J_h/M_h^2 = 0.72$ and 0.78, respectively. For magnetized FM tori surrounding Kerr BHs with spin parameters in the range 0.7-0.8, Table 2 of [29] suggests $\dot{E}/\dot{M}_0 \sim 0.9$ and $\dot{J}/(M_h \dot{M}_0) \gtrsim 2.0$. Thus, for accretion onto the central BH following collapse of star C, the values of \dot{E}/\dot{M}_0 and $\dot{J}/(M_h \dot{M}_0)$ are in rough agreement with the results of [29].

V. CONCLUSIONS

We have used a code which solves the GRMHD equations in dynamical spacetimes to simulate self-consistent disk formation and evolution following magnetized HMNS collapse. Our simulations extend the results of [19] by following the disk evolution for a much longer time, as well as by considering an alternative mag-

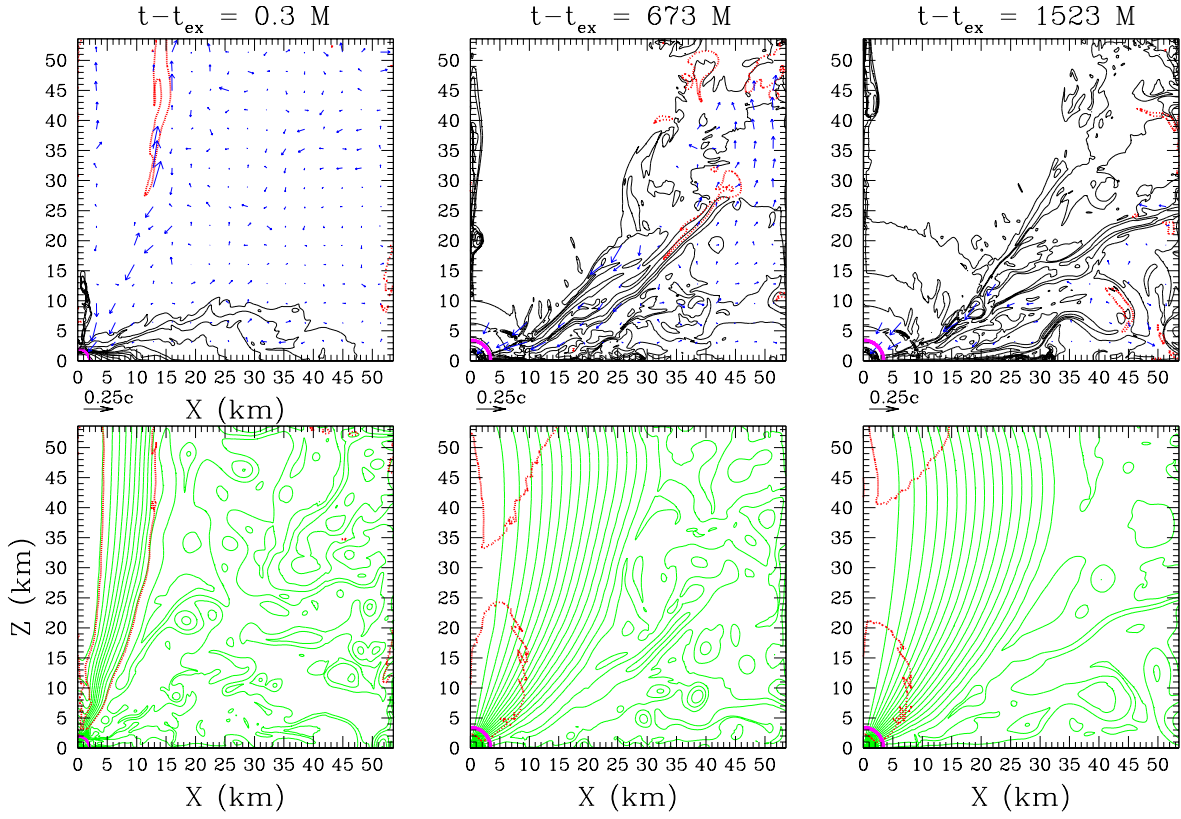


FIG. 11: Post-excision and Cowling evolution phases of case C2, shown at selected times. The meanings of the lines are the same as in Fig 5. The first and last sets of panels mark the beginning of the post-excision phase and the end of the simulation, respectively. The middle panels show an intermediate time during the Cowling phase. We note that the density feature near the rotation axis is not outbound or unbound, and thus does not constitute a jet.

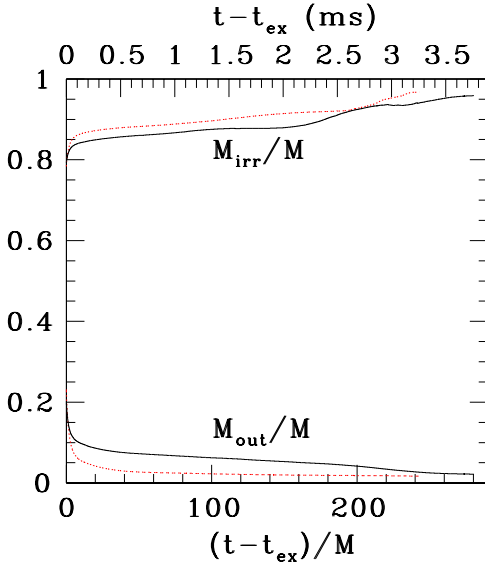


FIG. 12: Irreducible mass and rest mass outside the apparent horizon (normalized by the ADM mass at $t = 0$) for cases C1 (dashed red line) and C2 (solid black line). Notice that the mass remaining outside the apparent horizon decreases much more quickly for case C2 than for C1.

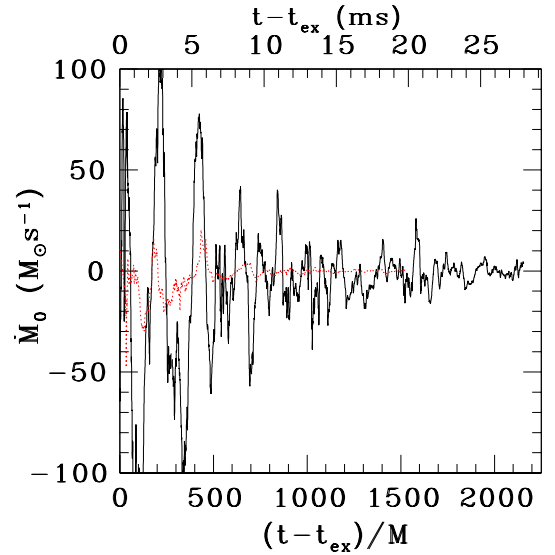


FIG. 13: Rest mass flux through a spherical shell located at $r = 12.2M = 47.7$ km for cases C1 (solid black line) and C2 (dashed red line). This plot covers both the post-excision and Cowling phases.

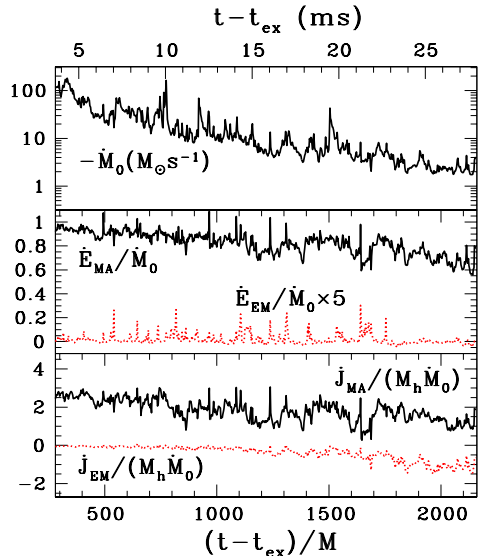


FIG. 14: Fluxes through the apparent horizon for case C1 during the Cowling phase. The lines have the same meaning as in Fig. 6. Here, however, the electromagnetic contribution to the angular momentum flux in the lower panel is not multiplied by a factor in order to make it visible on the plot.

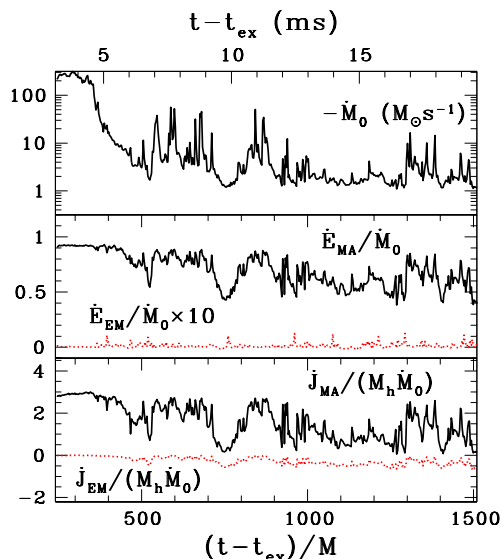


FIG. 15: Same as Fig. 14 for case C2.

netic field geometry [see Eq. (38)]. We evolve two HMNS models: star A with the simple Γ -law EOS of the form $P = (\Gamma - 1)\rho\epsilon$ with $\Gamma = 2$, and star C with the more realistic hybrid EOS given by Eqs. (14) and (15). Following collapse, star A quickly reaches a quasi-stationary accretion state, with very little matter ejected from the system or churned up into the corona. No significant outflow is observed from this system aside from a brief transient. This is likely due to the stiff EOS, which suppresses the formation of an extended corona. Without

significant fluid and magnetic field above the disk, the funnel wall outflow mechanism does not operate.

We considered two cases for the star C hypermassive model. Case C1 develops significant outflows along the boundary between the corona and the magnetically dominated funnel region near the axis. These outflows are triggered by reconnection across this boundary and the buoyant rising of the released field lines and matter. These outflows die down as the corona is gradually accreted. In contrast, case C2 develops no significant outflows. This model has a more extended initial magnetic field than C1, and thus the newly formed BH in the C2 case rapidly accretes most of the material remaining outside the apparent horizon, leaving little material left to the disk and corona. Since the outflow mechanism depends on interactions between the funnel and corona, outflows are suppressed in this case. We thus find that the presence of a funnel wall outflow is sensitive both to the EOS and to the initial magnetic field configuration.

As described in detail in [18], the remnant disk from the collapse of star C may produce enough energy to power a short GRB through neutrino-antineutrino annihilation alone. However, we have also shown that the collapse results in the formation of a magnetically dominated funnel, and the subsequent disk evolution (in the case of C1) leads to a funnel-wall outflow. The similarity of this morphology to previous studies of magnetized accretion disks [29, 31] suggests that a Poynting dominated outflow in the funnel region may also be expected. That we do not see this feature may be due to the numerical difficulty of handling magnetically dominated regions, especially in a GRMHD code for dynamical spacetimes (as discussed in [20]), and warrants further study. In any case, a fully realistic evolution in this region requires more sophisticated treatment of microphysical processes (such as pair creation) and careful consideration of regions where the ideal MHD approximation may break down [34, 51]. If the Blandford-Znajek process [57] does drive a Poynting-dominated outflow in the funnel region, the expected luminosity is [18, 58]

$$L_{\text{BZ}} \sim \text{few} \times 10^{53} a^2 (B/10^{16} \text{ G})^2 (M/2.6M_\odot)^2 \text{ erg/s}. \quad (39)$$

This luminosity would easily satisfy the typical energy budget for a short GRB and would likely dominate the $\nu\bar{\nu}$ pair annihilation luminosity, which should be $L_{\nu\bar{\nu}} \sim 10^{50}$ ergs/s [18, 58]. The mildly relativistic funnel wall outflow could play a role in collimating the inner fast jet [34], or even in stabilizing the jet against non-axisymmetric instabilities [59].

We also find that the magnetically dominated funnel region expands at late times in the simulation as the corona density and pressure drop. This could affect the opening angle at the base of a Poynting-dominated outflow. However, this emptying of the corona region may be due to the assumption of axisymmetry, since the corona depends on turbulent churning of the disk and the disk turbulence must decay by the anti-dynamo theorem [55]. Ultimately, self-consistent 3D simulations encompassing

the collapse and the subsequent disk and jet evolution will be required. However, our 2D results should be qualitatively correct before the disk turbulence begins to die down.

Acknowledgments

It is a pleasure to thank C. F. Gammie, J. C. McKinney, and S. C. Noble for useful suggestions and

discussions. Numerical computations were performed at the National Center for Supercomputing Applications at the University of Illinois at Urbana-Champaign (UIUC). This work was in part supported by NSF Grants PHY-0205155 and PHY-0345151, NASA Grants NNG04GK54G and NNG046N90H at UIUC.

-
- [1] B. Zhang and P. Mészáros, *Int. J. Mod. Phys. A* **19**, 2385 (2004); T. Piran, *Rev. Mod. Phys.* **76**, 1143 (2005).
- [2] R. Narayan, B. Paczynski, and T. Piran, *Astrophys. J. Lett.* **395**, L83 (1992); M. Ruffert and H.-T. Janka, *Astron. Astrophys.* **344**, 573 (1999).
- [3] J. S. Bloom, *et al.*, *Astrophys. J.* **638**, 354 (2006); E. Berger *et al.*, *Nature* **438**, 988 (2005); D. B. Fox, *et al.*, *Nature*, **437**, 845 (2005); J. Hjorth, *et al.*, *Nature*, **437**, 859 (2005).
- [4] T. W. Baumgarte, S. L. Shapiro, and M. Shibata, *Astrophys. J. Lett.* **528**, L29 (2000).
- [5] M. Shibata, T. W. Baumgarte, and S. L. Shapiro, *Astrophys. J.* **542**, 453 (2000).
- [6] I. A. Morrison, T. W. Baumgarte, S. L. Shapiro, and V. R. Pandharipande, *Astrophys. J.*, **610**, 941 (2004).
- [7] F. A. Rasio and S. L. Shapiro, *Astrophys. J.* **432**, 242 (1994); *Class. Quant. Grav.* **16** R1 (1999).
- [8] M. Shibata and K. Uryū, *Phys. Rev. D* **61**, 064001 (2000).
- [9] J. A. Faber and F. A. Rasio, *Phys. Rev. D* **62**, 064012 (2000).
- [10] M. Shibata, K. Taniguchi, and K. Uryū, *Phys. Rev. D* **68**, 084020 (2003).
- [11] M. Shibata, K. Taniguchi, and K. Uryū, *Phys. Rev. D* **71**, 084021 (2005).
- [12] M. Shibata, and K. Taniguchi, *Phys. Rev. D* **73**, 064027 (2006).
- [13] T. Zwerger and E. Müller, *Astron. Astrophys.* **320**, 209, 1997.
- [14] M. Rampp, E. Müller, and M. Ruffert, *Astron. Astrophys.* **332**, 969 (1998); H. Dimmellemeier, J. A. Font, and E. Müller, *Astron. Astrophys.* **388**, 917 (2002); **393**, 523 (2002); M. Shibata and Y. Sekiguchi, *Phys. Rev. D* **69**, 084024 (2004); C. D. Ott, A. Burrows, E. Livne, and R. Walder, *Astrophys. J.* **600**, 834 (2004).
- [15] Y. T. Liu and L. Lindblom, *Mon. Not. R. Astron. Soc.* **324**, 1063 (2001); Y. T. Liu, *Phys. Rev. D*, **65**, 124003 (2002).
- [16] M. D. Duez, Y. T. Liu, S. L. Shapiro, and B. C. Stephens, *Phys. Rev. D* **69**, 104030 (2004).
- [17] M. D. Duez, Y. T. Liu, S. L. Shapiro, M. Shibata, and B. C. Stephens, *Phys. Rev. Lett.* **96**, 031101 (2006).
- [18] M. Shibata, M. D. Duez, Y. T. Liu, S. L. Shapiro, and B. C. Stephens, *Phys. Rev. Lett.* **96**, 031102 (2006).
- [19] M. D. Duez, Y. T. Liu, S. L. Shapiro, M. Shibata, and B. C. Stephens, *Phys. Rev. D*, **73**, 104015 (2006).
- [20] M. D. Duez, Y. T. Liu, S. L. Shapiro, and B. C. Stephens, *Phys. Rev. D* **72**, 024028 (2005).
- [21] M. Shibata and Y.-I. Sekiguchi, *Phys. Rev. D* **72**, 044014 (2005).
- [22] L. Antón, O. Zanotti, J. A. Miralles, J. M. Martí, J. M. Ibáñez, J. A. Font, and J. A. Pons, *Astrophys. J.* **637**, 296 (2006).
- [23] M. Anderson, E. Hirschmann, S. L. Liebling, and D. Neilsen, *Class.Quant.Grav.* **23** 6503 (2006); D. Neilsen, E. W. Hirschmann, and R. S. Millward, *Class. Quant. Grav.* **23**, S505 (2006).
- [24] B. Giacomazzo and L. Rezzolla, *Class. Quant. Grav.* **24**, S235 (2007).
- [25] H. C. Spruit, *Astron. and Astrophys.*, **349**, 189 (1999)
- [26] S. L. Shapiro, *Astrophys. J.* **544**, 397 (2000).
- [27] V. P. Velikhov, *Soc. Phys. JETP*, **36**, 995 (1959); S. Chandrasekhar, *Proc. Natl. Acad. Sci. USA*, **46**, 253 (1960).
- [28] S. A. Balbus and J. F. Hawley, *Rev. Mod. Phys.* **70**, 1 (1998).
- [29] J. C. McKinney and C. F. Gammie, *Astrophys. J.*, **611**, 977 (2004).
- [30] L. G. Fishbone and V. Moncrief, *Astrophys. J.*, **207**, 962 (1976).
- [31] J.-P. De Villiers, J. F. Hawley, and J. H. Krolik, *Astrophys. J.* **599**, 1238 (2003).
- [32] J.-P. De Villiers, J. F. Hawley, J. H. Krolik, and S. Hirose, *Astrophys. J.* **620**, 878 (2005).
- [33] J.-P. De Villiers, J. Staff, and R. Ouyed, *astro-ph/0502225* (2005).
- [34] J. C. McKinney, *Mon. Not. Roy. Astron. Soc.* **368**, 1561 (2006).
- [35] Y. Mizuno, K.-I. Nishikawa, S. Koide, P. Hardee, and G. J. Fishman, *astro-ph/0609344* (2006).
- [36] S. Koide, K. Shibata, T. Kudoh, and D. L. Meier, *Science* **295**, 1688 (2002).
- [37] M. Shibata and T. Nakamura, *Phys. Rev. D* **52**, 5428 (1995); T. W. Baumgarte and S. L. Shapiro, *Phys. Rev. D* **59** (1999), 024007; see also T. Nakamura, K. Oohara, and Y. Kojima, *Prog. Theor. Phys. Suppl.* **90**, 1 (1987).
- [38] M. Alcubierre, S. Brandt, B. Brügmann, D. Holz, E. Seidel, R. Takahashi and J. Thornburg, *Int. J. Mod. Phys. D* **10**, 273 (2001).
- [39] M. D. Duez, S. L. Shapiro, and H.-J. Yo, *Phys. Rev. D* **69**, 104016 (2004).
- [40] B. J. van Leer, *J. Comput. Phys.* **23**, 276 (1977).
- [41] A. Harten, P. D. Lax, and B. J. van Leer, *SIAM Rev.* **25**, 35 (1983); B. Einfeldt, *SIAM J. Numer. Anal.* **25**, 294 (1988).
- [42] G. Tóth, *J. Comput. Phys.* **161**, 605 (2000); C.F. Gammie, J.C. McKinney, and G. Tóth, *Astrophys. J.* **589**,

- 444 (2003).
- [43] A. Akmal, V. R. Pandharipande, and D. G. Ravenhall, Phys. Rev. C **58**, 1804 (1998); F. Douchin and P. Haensel, Astron. Astrophys. **380**, 151 (2001).
- [44] J. A. Font, M. Miller, W.-M. Suen, and M. Tobias, Phys. Rev. D **61**, 044011 (2000).
- [45] M. Shibata, Y.T. Liu, S.L. Shapiro, and B.C. Stephens, Phys. Rev. D, **74**, 104026 (2006).
- [46] R. M. Wald, *General Relativity* (Univ. of Chicago, Chicago, 1984), p. 297.
- [47] A. Ashtekar, and B. Krishnan, Living Rev. Relativity, **7**, 10 (2004) (<http://www.livingreviews.org/lrr-2004-10>); O. Dreyer, B. Krishnan, D. Shoemaker, and E. Schnetter, Phys. Rev. D, **67**, 024018 (2003).
- [48] M. Ansorg, J. Math. Phys. **39**, 5984 (1998).
- [49] C. F. Gammie, J. C. McKinney, and G. Tóth, Astrophys. J., **589**, 444 (2003).
- [50] G.B. Cook, S.L. Shapiro, and S.A. Teukolsky, Astrophys. J., **398**, 203 (1992).
- [51] J. C. McKinney, astro-ph/0506369 (2005).
- [52] L. Baiotti and L. Rezzolla, Phys. Rev. Lett. **97**, 141101 (2006).
- [53] J. A. Faber, T. W. Baumgarte, Z. B. Etienne, S. L. Shapiro, K. Taniguchi, Phys. Rev. D, in press (arXiv:0708.2436v2 [gr-qc]).
- [54] S. S. Komissarov and M. V. Barkov, arXiv:0707.0264 (2007).
- [55] H. K. Moffatt, *Magnetic Field Generation in Electrically Conducting Fluids* (Cambridge Univ. Press, 1978); J. F. Hawley, C. F. Gammie, and S. A. Balbus, Astrophys. J. **440**, 742 (1995); J. F. Hawley, Astrophys. J. **528**, 462 (2000).
- [56] A. Mignone and J. C. McKinney, arXiv:0704.1679 (2007).
- [57] R. D. Blandford and R. L. Znajek, Mon. Not. R. astr. Soc. **179**, 433 (1977).
- [58] Di Matteo, R. Perna, and R. Narayan, Astrophys. J. **579**, 706 (2002).
- [59] Y. Mizuno, P. Hardee, and K.-I. Nishikawa, Astrophys. J. **662**, 835 (2007).